PCCP

Accepted Manuscript

ROYAL SOCIETY OF CHEMISTRY

www.rsc.org/pccp

PCCP

ARTICLE

Influence of mixed organic cation ratio in lead iodide based perovskite on the performance of solar cells

Received 00th January 20xx,
Accepted 00th January 20xx

DOI: 10.1039/x0xx00000x

www.rsc.org/

Manuel Salado[a] Laura Calio, Ruediger Berger[b], Samrana Kazim*[a], Shahzada Ahmad*[a]

Lead halide based perovskite solar cells are presently the flag ship among the third generation solution-processed photovoltaic technologies. The organic cation part in the perovskite play an important role in terms of crystal structure tuning from tetragonal to trigonal or pseudocubic or vice versa depending on the organic cations used, while it also display different microstructure. In this paper, we demonstrate the influence of the organic cation part with respect to optical properties, hysteresis behavior, and stability. This study elucidates a clear understanding about the perovskite properties and how they can be modulated by compositional engineering. With a rational choice, light harvesting abilities and hysteresis behavior can be controlled in these systems. The fractional substitution of formamidinium cation by methylammonium cation allows achieving low temperature annealing and inducing stability in perovskites together with enhanced photovoltaic properties. By the use of in situ-scanning force microscopy experiments the conversion of precursors to perovskite formation at a particular temperature can be visualize.

Introduction

Since the discovery of the photovoltaic (PV) effect in the eighteenth century, researchers have shown keen interest in the development of cost effective and efficient materials to convert solar energy into electricity. Currently, major market share c.a 91% is being control by Silicon solar cells, among them mono crystalline silicon solar cells give the power conversion efficiencies (PCE) of >25%. Its high production cost and high usage of raw materials escalates its energy payback time and limits their wide application for grid parity. Over the last decades, different technologies such as dye-sensitized solar cells (DSSCs), organic solar cells and inorganic thin film based solar cells have been extensively studied mainly due to their low amount of material needs, being solution processable and cost competitiveness.[1]

In recent years, perovskite solar cells (PSCs), has stunned the PV field, by the tremendous research interest owing to their unique combination of high performance and low-cost fabrication process. Compared with the existing technology, PSCs have demonstrated its potential by establishing an unprecedented increment in the PCE from 3.8%[2] to >22% (http://www.nrel.gov/ncpv/) in a short time frame. The panchromatic light-absorption ability along with high absorption coefficient, tuneable direct band gap and charge separation and transport capability of the organohalide perovskite makes them suitable as light absorber material for PV applications.[3,4] However, one of the concerns that need to be addressed is the stability and hysteresis behaviour in the devices.[5] In a boarder term perovskite refers to any material which follows the crystal structure of ABX_3. In case of hybrid organic-inorganic perovskite, A and B corresponds to organic and inorganic cations respectively, while X represents the halide anion. In order to balance the charge in the structure, the organic cation (A) occupies the cuboctahedral cavity formed by eight PbI_6 octahedra. The size of the cation "A" can notably affect the symmetry of the octahedral network and alter the band gap.[6] Theoretically, It is known that the three-dimensional (3D) perovskite form when their tolerance factor (t) fall in the range of 0.7 to 1 as described by Goldschmidt.[7] Methylammonium ($CH_3NH_3^+$, MA, ionic radius 2.70 Å) and formamidinium ($HC(NH_2)^+$, FA, ionic radius 2.79 Å) both satisfy the tolerance factor (t) to form a 3D network. However, due to a slightly larger cation size than MA, FA, provides red shifting of the absorption onset due to change in metal-halide-metal bond angle and leads to a narrower band gap (1.48 eV)[8,9] compare to $MAPbI_3$ (1.57 eV).[10] Additionally, formamidinium lead iodide ($FAPbI_3$) shows almost equal or higher charge carrier mobility (~75 cm^2/Vs) than $MAPbI_3$ depending on the processing method,[11,12,13] better thermal stability at high temperature and negligible hysteresis during *J-V* measurements as compare to $MAPbI_3$.[9,14,15] However, it is difficult to prepare uniform, fully covered surface of stable

[a] Mr. M. Salado, Ms. L. Calio, Dr. S. Kazim*, Dr. S. Ahmad*
Abengoa Research
C/ Energía Solar nº 1, Campus Palmas Altas-41014, Sevilla, Spain
E-mail: shahzada.ahmad@abengoa.com
samrana.kazim@abengoa.com
[b] Dr. R. Berger
Max Planck Institute for Polymer Research,
Ackermannweg 10, Mainz 55128, Germany

photoactive black polymorph (α-phase) of $FAPbI_3$ perovskite due to its phase transition into yellow non perovskite (δ-phase) at room temperature. The conversion to α-phase of $FAPbI_3$ is achieved at high temperature (>140ºC).

The microstructure and phase purity of the thin film rely on the perovskite crystal formation processes. A variety of different deposition techniques have been used with the aim to achieve high quality perovskite layer, such as, two step (sequential deposition)[16], vacuum evaporation[17], vapour-assisted deposition[18] or recently developed solvent engineering approach.[19] To derived synergistic effect from both FA and MA organic cations's opto-electrical properties, one of the suggested alternatives was partial replacement of MA cation by FA. So far, only few studies have published for mixed organic cation of $MAPbI_3$ and $FAPbI_3$ using two-step sequential method.[14,20,21]

These mixed organic-cations exhibited PV performance superior to pure $MAPbI_3$, due to its extended absorption in the red part of the spectrum, better semiconducting properties and high structural and thermal stability provided by the incorporation of FA cation in the MAI lattice matrix.[14,20] The band gap can be tuned by changing the mixed cation ratio and it has been found that it varies by the perovskite processing method.[22] However, none of these studies addressed the hysteresis behaviour in the solar cells, which is crucial to understand the real figure of merit for PV devices.

In this paper, we have studied the structural, surface, optical, and photovoltaic properties of 3-dimensional mixed cation perovskites having a range of composition $MA_xFA_{(1-x)}PbI_3$ (x= 0-1) as light-harvesting material in a mesoscopic solar cells configuration. The mesoscopic configuration was found to be ideal for the formation of α-phase of $FAPbI_3$. By utilizing anti-solvent approach, during one step deposition process of perovskites, it is possible to obtain dense morphology with highly crystalline and large crystals in a mixed cations environment of MA and FA cations. This deposition method also allows us to transform the rough perovskite film into a smooth and glossy perovskite, with the aim to obtain homogeneous and high surface coverage with favourable interface. In this approach, non-polar solvents (e.g. toluene or chlorobenzene) which are miscible with perovskite precursor solution but do not dissolve perovskite film was used for dripping. PbI_2 and the mixture of MAI and FAI were used as perovskite precursor and dissolved in dimethylsulfoxide (DMSO). During the preparation of this article, Jacobsson et al. reported mixed cation (FA and MA) and anion (Br and I) based perovskite using one step solvent engineering method.[23] In our study only mixed cation were used with the composition $MA_xFA_{(1-x)}PbI_3$ (x= 0-1) and prepared by one step solvent engineering method showing good air stability and less hysteresis in case of some selected composition. An array of techniques was employed to characterize the devices in order to unravel the physical and electrical properties of the perovskite solar cells and its hysteresis behaviour.

Results and discussion

X-ray diffraction measurements were made to investigate the phase purity of mixed cation perovskite and incorporation of FA cation into $MAPbI_3$ perovskite lattice. The XRD spectra were recorded for all mixed organic cation perovskites $MA_xFA_{(1-x)}PbI_3$, (x=0−1) and shown in Figure 1. The perovskite film was deposited onto coarse glass as substrate and measured after annealing the sample for one hour at 100ºC, for x=0.6 to1 and at 120ºC , 150ºC for x=0.5 and x=0 respectively. At room temperature, pure $MAPbI_3$ has a tetragonal structure while $FAPbI_3$ (black α-phase) has a cubic structure due to slight rotation of lead iodide octahedra.[10,24] The main diffraction peaks in pure $MAPbI_3$, where structural changes were detected, were found at ~14º, 19.95º, 24.41º, 28.5º and 31.9º and belong to characteristic peak of a tetragonal perovskite structure while peaks at 13.7º and 27.8º in pure $FAPbI_3$ correspond to cubic black stable phase of α-$FAPbI_3$.[24] The peak present at 12.63º reflects the presence of non-converted PbI_2, for which the intensity decreases in mixed cation (x=0−1) environment except in $MA_{0.5}FA_{0.5}PbI_3$ perovskite which shows strong peak of PbI_2.

Figures S1a-c, are focused on the characteristic peaks of tetragonal structure of perovskite. The peaks at 14.17º, 28.33º and 31.9º gradually shift to the lower diffraction angle (2θ) with increasing amount of FA cation. Mainly due to relatively large size of the FA cation causes the lattice expansion. Instead of appearance of separate and individual two peaks with different intensity of two cations, the slow shifting in diffraction angle indicates the presence of a mixed phase, where both cations were incorporated in the same lattice.

On closer visualization into the characteristic tetragonal peak at 14º, the high intense and narrow peak was observed in case of $MAPbI_3$, which suggest its larger crystallite size than mixed cation perovskite. (Figure S2) represents the calculated average crystallite size calculated by XRD software versus FA composition. The intensity of peak decreases with increasing amount of FA in $MA_xFA_{(1-x)}PbI_3$(x= 0-1) while the full width half maximum (FWHM) increases up to x=0.85 in $MA_xFA_{(1-x)}PbI_3$, while in the case of x=0.5, FWHM decreases. The decrease in FWHM indicates an increase of X-ray crystallite size. For pure $FAPbI_3$, the FWHM was found to be the highest. (Figure S1a)

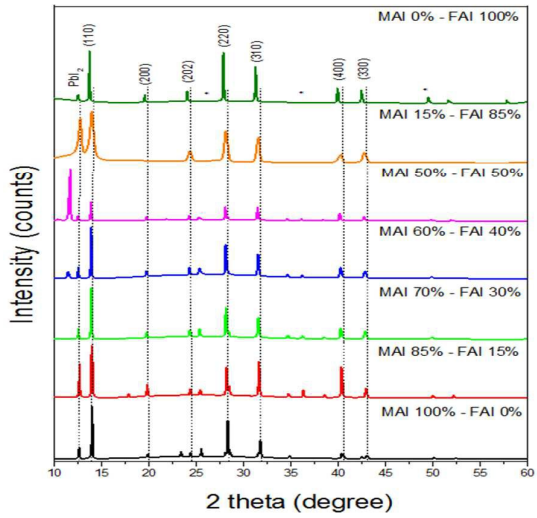

Figure 1. X-ray diffraction spectra for the $MA_xFA_{(1-x)}PbI_3$ perovskite film, where (x=0, 0.15, 0.5, 0.6, 0.7, 0.85, 1). These films were annealed for one hour at 100 ºC for x=0.6 to 1, at 120ºC for x=0.5 while, 150 ºC for x=0 and 0.15. The closer view of characteristic peak at 14.17º, 28.33º and 31.9º is shown in Figure S1.

In mixed cation perovskite, $MA_xFA_{(1-x)}PbI_3$ (x=0.85–0.6), no characteristic diffraction peak of δ-phase of $FAPbI_3$ was observed (which is photo-inactive phase) except in x=0.5, where high intense peaks at 11.7º represents δ-phase of $FAPbI_3$[20,25]. It is well known that, annealing temperature of the perovskite affects its final structure and its electro-optical properties. In pure methylammonium iodide (MAI) conversion to perovskite take place between 80–100ºC while in the case of formamidinium black α-phase perovskite formed at 135-150 ºC.[26,27] It is worth to mention that δ-phase of formamidinium is present only in 50:50 ratio; which might be due to the un sufficient annealing temperature required to convert into black α-phase of $FAPbI_3$. Due to the higher amount of $FAPbI_3$ in $MA_{0.5}FA_{0.5}PbI_3$, these crystals do not confined into the mesoporous scaffold which is limiting the crystallite size ~50 nm, therefore these crystals randomly arrange themselves on the surface of mesoporous scaffold rather than goes inside and thus form large crystallite.[10] Bein et al[20] studied the stabilization of the trigonal high-temperature phase of formamidinium lead iodide. It was shown that crystal structure of MA degrades at 125°C, however black α-phase formed at a higher temperature (135°C). Therefore we assume that, annealing temperature takes an important part in the preparation of mixed organic cation perovskites. In order to reveal the optimal temperature of annealing in the $MA_{0.5}FA_{0.5}PbI_3$, it was heated at different temperatures (120°C, 135°C and 150°C) and measured X-ray diffraction and absorption spectra (Figure S3 and S4). From XRD (Figure S3), It can be seen that at 120°C, the strong peak were present at ~14° corresponds to tetragonal structure of $MAPbI_3$ along with the strong peak at ~12° indicating that PbI_2 is not fully converted to perovskite. On increasing the temperature to 135°C, the peak at ~14° becomes less intense which finally disappear on reaching the annealing temperature to 150°C indicating degradation of $MAPbI_3$ phase. At 135°C and 150°C, the emergence of the peak at ~11° confirms the presence of δ-phase of $FAPbI_3$ and peak corresponds to PbI_2 get more intense at this stage. The inadequate conversion into perovskite phase indicates presence of thermodynamically stable point beyond which the substitution of FA does not occur.[10] The presence of yellow δ-phase of $FAPbI_3$ as observed in XRD also coincides with the SEM images of the perovskite shown in supporting information (Figure S5). The white crystals on the surface can be observed at 135°C and their number increases on increasing the temperature to 150°C. Recently similar observation was reported[10,20]. This may be assigned to the preferred yellow phase of $FAPbI_3$ at room temperature. However, in absorption measurements (Figure S4), we do not observe any significant changes except that the absorbance intensity of $MA_{0.5}FA_{0.5}PbI_3$ decreases in case of annealed samples at 135°C and 150°C, which might be due to the conversion of δ-phase yellow perovskite. In our conditions we found that the optimal annealing temperature for this ratio was 120°C (Figure S3), avoiding the degradation of MA cations in the matrix. Nevertheless, the shape and the size of the crystals depends on the mixed cation perovskite ratio to dictate the final performance of the perovskite solar cells.[25]

The conversion of the precursors into perovskite can be observed and confirmed by absorption spectra of mixed organic cation perovskite. Perovskite films were deposited onto mesoporous TiO_2 layer to evaluate the crystal growth same as in devices. Figure 2 shows the absorption spectra of mixed cation perovskite measured with integrating sphere for all different compositions. A systematic shift of the absorption band edge to longer wavelengths was observed with increasing amount of the FA cation in $MA_xFA_{(1-x)}PbI_3$ perovskite film, where (x=0 to 1). The addition of FA cation red shifts the absorption onset from 780 nm in pure $MAPbI_3$ to 815 nm in the case of pure $FAPbI_3$. Thus the energy band gap (E_g) can be easily tuned by varying the mixed cation ratio and can be shifted towards longer wavelength. For mixed cation perovskite with x=0.5 and pure $FAPbI_3$, the absorbance decreases with increasing wavelength than other compositions.

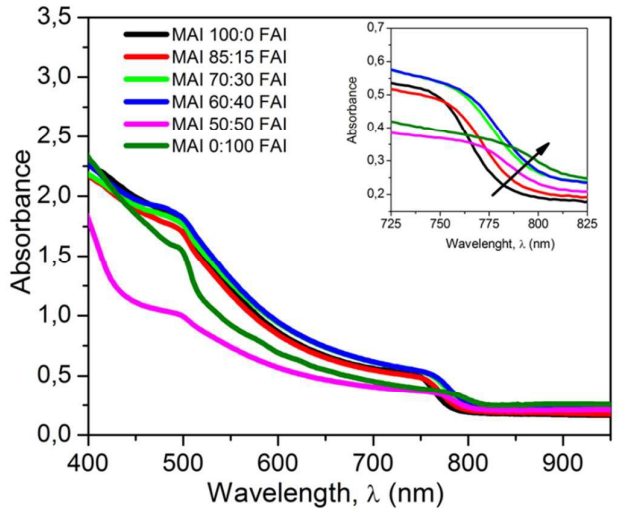

Figure 2. UV-Vis absorbance spectra of a perovskite $(MA)_x(FA)_{1-x}PbI_3$ layer on FTO including compact and mesoporous TiO_2.

Maximum absorbance was observed for $MA_{0.6}FA_{0.4}PbI_3$ perovskite, with red-shift extension of the absorption onset. Figure 3 shows the linear dependence of the optical band gap on added FA cation composition in $MA_xFA_{(1-x)}PbI_3$ perovskite film, where (x=0 to 1). As the amount of FA cation is increased in $MAPbI_3$ lattice, the band gap decreases from 1.59 eV (pure $MAPbI_3$) to 1.5 eV for pure $FAPbI_3$, while the mixed cation showed the intermediate value between 1.59 to 1.5eV. It is to be mentioned that these perovskite films were prepared on mesoporous TiO_2, thus due to perovskite confinement into mesoporous, it may affects the crystal structure of perovskite and thus its band gap.[21,28]

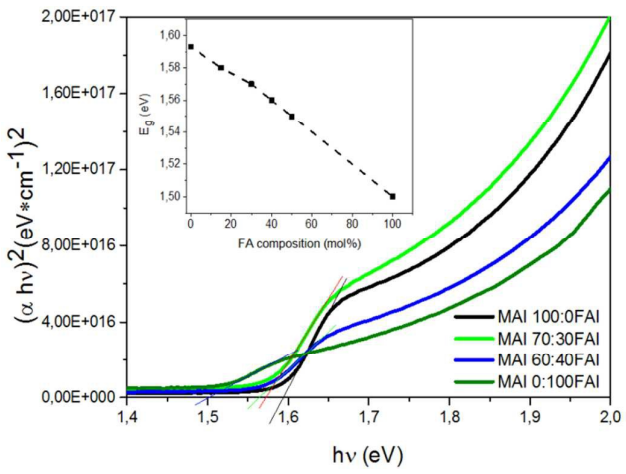

Figure 3. Tauc plots for perovskite(MA)x(FA)1-xPbI_3 (x=0, 0.6, 0.7, 1) and inset shows all compositions (x=0, 0.5, 0.6, 0.7, 0.85, 1) value of the band gap (eV) plotted versus amount of formamidinium added in molar percentage.

For calculating optical band gap, the absorption coefficient (α) was calculated by measuring total transmittance and reflectance spectra using integrating sphere. Then Tauc plot method was applied to estimate the direct band gap, i.e. linear extrapolation of $(\alpha h\upsilon)^2$ vs hυ curve to intercept the horizontal energy axis for those shown in Figure 3.

An optimal ratio exists for compromise between absorption shift and perovskite crystal quality, will be explained in the following sections. The morphologies of the mixed perovskites were characterized by scanning electron microscopy (SEM) and scanning force microscopy (SFM) in order to visualize the crystallization process and distribution of grains in different composition of MAI:FAI. The perovskite film was deposited atop of a mesoporous layer to reproduce the similar crystal growth as in devices. Figure 4 shows the surface microstructure of the pure $MAPbI_3$, $FAPbI_3$, the $MA_{0.6}FA_{0.4}PbI_3$ and the cross sectional image of $MA_{0.6}FA_{0.4}PbI_3$ perovskite based device.

Figure S5 and S6 represents SEM images of the remaining composition. The morphology of the perovskite significantly changes with inclusion of FA cation. SEM images depict adequate surface coverage and densely packed grains with less number of pinholes. In case of $FAPbI_3$, crystal edges were observed which lead to the formation of lamellar like structures. Furthermore the grain size varies with the MA:FA composition in perovskite. The crystallite size was larger in case of pure $MAPbI_3$ and $FAPbI_3$ perovskite as confirmed by XRD measurements showing narrow peak. Small sized, more compact, regular and ordered crystallites with preferential orientation were observed with an average crystallite size ranging from 60−62 nm (Figure S2) in case of x=0.7, 0.6 and in close agreement of literature value.[29] These crystallites are much smaller than the size observed by SEM indicating that these crystals are composed of several small grains. It is reported that during the crystallization process, if there is no lattice strain in the structure, it leads to the formation of large crystals due to more relaxation in crystal lattice[30,31] as shown in XRD measurements where peak shifted to lower angle with increasing amount of FA cation. Pure $MAPbI_3$, $FAPbI_3$ and $MA_{0.85}FA_{0.15}PbI_3$ shows the larger crystallite size as calculate by the XRD measurements.

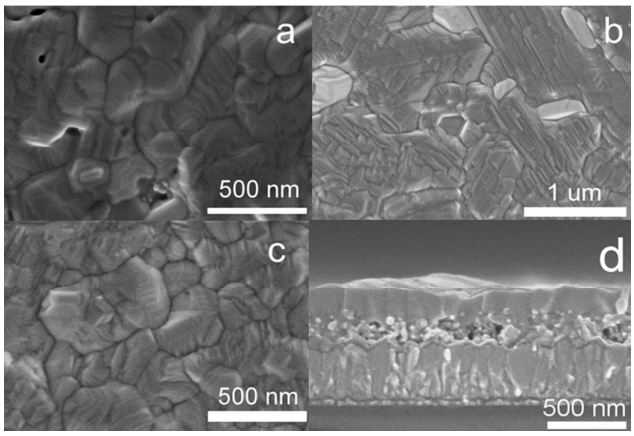

Figure 4. (a-c) SEM images of different organic cations ratio perovskite films ($MAPbI_3$, $FAPbI_3$ and $MA_{0.6}FA_{0.4}PbI_3$ respectively) and (d) cross section image of

TiO_2/$MA_{0.6}FA_{0.4}PbI_3$/Spiro-OMeTAD solar cell. Figure a, b and c reveal the morphology evolution of the perovskite films when the organic cation composition was changed.

As the amount of FAI increases in $MAPbI_3$ lattice; the lattice strain increases due to comparatively larger cation size of FA and crystallization slowed down and consequently, the small crystals were formed in case of x=0.7, 0.6 (60–62 nm) and confined to the pores of mesoporous scaffold with preferential orientation and high degree of order.[32] The improved and controlled crystallization of perovskite film may reduce the density of defects and the quality of perovskite crystals can affect the charge carrier diffusion length, efficiency of charge dissociation and transport.[33-45] Subsequently, this will influence the performance of the devices due to presence of defects which creates the trapping site for recombination of electrons and holes. Therefore the larger crystals at the interface are beneficial owing to a reduction of grain boundaries and trap sites and they also act as scattering centers for the incoming light and increase the effective optical path length of light in the device.

Notably, in some of the perovskite compositions, more specifically, in $MA_{0.5}FA_{0.5}PbI_3$ and pure $FAPbI_3$, individual grains exhibit higher brightness compared with the adjacent area. Figure S3 shows the SEM images of $MA_{0.5}FA_{0.5}PbI_3$ with different annealing temperature. It can be observed that bright contrast was present in all the perovskite samples annealed at different temperature. In all like hood, this can be possibly originated due to non-perovskite δ-phase of $FAPbI_3$, which was also confirmed by the XRD measurement made at different annealing temperature.

To investigate the role of annealing temperature on perovskite film morphology and its crystal formation, we performed SFM while in-situ heating of a mixed perovskite film. We observed that the 60:40 ratio shows almost negligible hysteresis in *J-V* measurements. Therefore, in this study, we used a mixed perovskite $MA_{0.6}FA_{0.4}PbI_3$ (60:40 molar ratio) film for SFM. It is well known fact that, perovskites is sensitive to temperature and moisture[46,47].

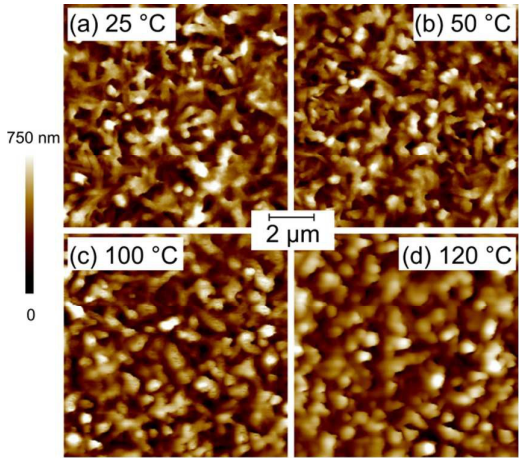

Figure 5: SFM topographic of the FTO/$MA_{0.6}FA_{0.4}PbI_3$, during in-situ temperature annealing. The images were recorded at a) 25, b) 50, c) 100 and 120ºC. At each temperature we waited 20 minutes to allow the sample to thermally equilibrate.

Pure methyl ammonium iodide (MAI), at room temperature forms an active β-phase. At around 55–60ºC, this active β-phase is converted into α-$CH_3NH_3PbI_3$.

At the initial stage, i.e. prior to annealing, the deposited layer formed a surface with a root-mean-square (rms) roughness of 147 nm at a 10×10 μm^2 scale. The deposited layer showed a 3-dimensional network like structure (Figure 5a). On increasing the temperature to 50°C we observed closing of the pores, and we attribute to the intercalation induced volume expansion of inorganic materials in organic phase. Upon further annealing to 100°C and 120°C clear visible changes was observed, (Figure 5c and d). This abrupt microstructural changes reflects the conversion of the deposited layer into the perovskite structure, which is very prominent at or above 100°C.

Photovoltaic properties

To calculate the figure of merit for the fabricated PV devices, the *J-V* curves were recorded in dark and under simulated air mass 1.5 global (AM1.5G) sunlight. Figure 6 shows the *J-V* characteristics in dark and under illumination at 100 mW/cm^2 for the best performing devices in reverse direction (From V_{oc} to J_{sc}) at 100 mV/s. Table 1 summarizes the average PV parameters with standard deviation along with the best-performing devices prepared for different composition of MAI:FAI together with series and shunt resistance. The increase in short circuit current (J_{sc}) after the inclusion of FA in $MA_xFA_{(1-x)}PbI_3$ perovskite can be observed, which was expected due to shifting of absorption onset to longer wavelength. The average Jsc and fill factor (FF) increased gradually from 19.57 to 21 $mAcm^{-2}$ and from 64.8 to 70% respectively with increasing the FA concentration from 0 to 40 mol%. The lowest value for short circuit current (J_{sc}) was observed for $MA_{0.5}FA_{0.5}PbI_3$, $MA_{0.15}FA_{0.85}PbI_3$ and pure $FAPbI_3$, which coincide with the optical absorption of these two perovskite (Figure 2). A drop in V_{oc} was observed on increasing the concentration of FA beyond 40%, for pure $MAPbI_3$ shows a V_{oc} of 950 mV, while the lowest V_{oc} was obtained in the case of pure $FAPbI_3$ (V_{oc}=750 mV). In case of pure $FAPbI_3$, the V_{oc} drop might be due to the presence of non-perovskite δ-phase which destroys the crystal lattice and crystal structure of perovskite hence modify the band gap.[21,28] While in case of $MA_{0.6}FA_{0.4}PbI_3$ ratio, the high value of V_{oc} could be related to the better confinement of the small sized perovskite crystals to the pores of mesoporous scaffold with preferential orientation and high degree of order.[32]

Similarly, the low FF was observed in case of $MA_{0.5}FA_{0.5}PbI_3$, $MA_{0.15}FA_{0.85}PbI_3$ and in pure $FAPbI_3$, due to the presence of yellow δ-phase of $FAPbI_3$ causing the sudden drop in PV performance. This feature can be related with the increase in series resistance and decrease in shunt resistance (Figure S8). The series and shunt resistance were evaluated using the software from the slope of *J-V* curve and reported in Table 1. We have observed decrease in series resistance, while increase in shunt resistance for up to 40 mol% of FA cation, which can be related to the increased grain size of the perovskite and

better confinement of perovskite inside the pores for intimate connectivity with TiO_2 layer.[9]

The size of the grain is increased with the inclusion of $FAPbI_3$, which further decreases up to a certain concentration of FAI (40 mol%, x=0.6) and beyond that concentration, the grain size again increases for $MA_{0.5}FA_{0.5}PbI_3$ and pure $FAPbI_3$ (x=0.5, and 0) as confirmed by the XRD and SEM studies. Change in series and shunt resistance values is correlated with the morphological changes in mixed perovskite after inclusion of $FAPbI_3$. It is reported that the large-sized grain reduces the grain boundaries and thus series resistance might be decrease. Similarly, decrease in shunt resistance might be a result of shunting pathway created due to the inadequate connectivity between the blocking layer and perovskite interface. The decreased V_{oc} and low FF point towards the high charge recombination losses along with low shunt resistance and high series resistance in case of x=0.5-0.[48] Pure $MAPbI_3$ based devices gave good performance; however, it suffered from hysteresis behaviour (Table S1). It can be deduced from the Figure 6 that there is an improvement in the average PCE in the case of mixed perovskite compare to pure MAI (η=12.11±0.97%) or pure FAI (5.42±1.00%). An improve PCE was achieved for $MA_{0.85}FA_{0.15}PbI_3$ (η=13.62±0.42%), however $MA_{0.6}FA_{0.4}PbI_3$ gave best PV performance.

One of the main concerns in perovskite solar cells behavior is the presence of hysteresis in the current-voltage curve depending on the measurement direction (forward or reverse) and scan rate.[49-51]

J-V curves were measured at various scan rates for both reverse and forward directions at different dwell time and we found that in our case, 100mV/s was the optimized scan rate.

Hysteresis effect has been quantified as hysteresis index as reported by Kim et al. (Table S1). The *J-V* curves were measured at 100 mV/s to calculate the degree of hysteresis (Figure S7) and the corresponding values of PV parameters and HI are given in Table S1. Hysteresis index can be lowered by increasing the FAI ratio. It was found that the degree of hysteresis decreases with increasing amount of FAI up to 40mol%. Beyond this composition, the degree of hysteresis increases.

A rational match can be obtained for $MA_{0.6}FA_{0.4}PbI_3$, where the PCE is the best with a negligible degree of hysteresis. The lowest series resistance was noticed in $MA_{0.85}FA_{0.15}PbI_3$ which is justified by its high fill factor and performance. Hysteresis behaviour in the perovskite solar cells are generally associated with high capacitances (on the order of mF/cm^2) compared to Si cells (in the order of $\mu F/cm^2$).[52] This capacitance effect was attributed by some authors to (i) the ferroelectricity or polarization of the perovskite layer; (ii) contact conductivity; (iii) diffusion of excess ion as interstitial defects; and/or (iv) trapping/de-trapping of charge carriers.

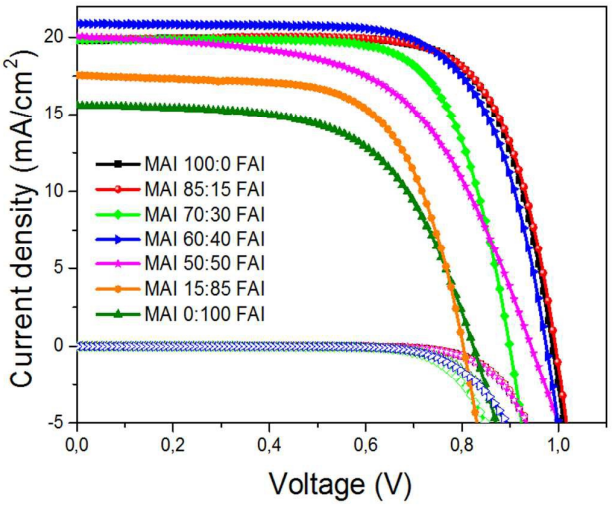

Fig.6: J-V characteristics for mesoscopic devices with mixed cation perovskite $MA_xFA_{(1-x)}PbI_3$ where (x=0, 0.5, 0.6, 0.7, 0.85, 1) as light absorber under 100 mW/cm^2 AM 1.5G irradiation. Active area: 0.16 cm^2, scan rate: 100 mV/s, and the scan direction was reverse that is from V_{oc} to J_{sc}.

Even though recent studies, pointed ion migration (I^- and MA^+) and charge trapping at interface as a presumptive cause of the hysteresis in perovskite solar cells, however, the mechanism of ion transportation and origin of these traps is still scarcely understood.[51,53] Recently, reports on generation of ion migration channels[54] is reported. One of them is the local lattice distortion due to confinement in mesoporous scaffold. Mostly 70% of pure $MAPbI_3$ within mesoporous scaffold was found to be disordered with more lattice defect, which is undetectable in XRD measurement.[55] This may explain severe photocurrent hysteresis in mesoporous devices in addition to the trapping effect. In our case, the calculated crystallite size was least in x=0.6, 0.7 (60–62 nm) which shows the better confinement into scaffold and probably preferred orientation with less distortion in lattice and thus experiencing negligible hysteresis. While in case of larger crystals size in the remaining composition studied here, comparatively high degree of hysteresis was observed. However, the local rearrangement of charges at the interfaces or in defects in the perovskite layer could give rise to commonly observed capacitive effects. Nevertheless, the existence of ionic vacancies is influenced by the process adopted for crystal growth.[54]

To further elucidate the device performance, we measured the devices at different scan rate in both the forward and reverse direction and almost negligible hysteresis can be identified in some devices. In other words, the hysteresis behaviour could be controlled by finding a proper ratio which implies that the desirable crystal formation is obtained as well as in the reduction of trap sites. Figure S7 exhibits current density-voltage (*J-V*) curves in reverse and forward direction to see the hysteresis depending on the organic cation ratio perovskite based solar cells. Hysteresis behaviour is related with crystal size and the grain boundaries in perovskite layer, however, shape and direction of the crystal growth induce the creation

of traps states on the perovskite structure.[25,56] In accordance with the absorbance measurements, the inclusion of formamidinium cation results in shifting IPCE onset towards longer wavelength (inset Figure 7). By increasing the FAI concentration, it is expected to absorb more light in the near IR part of the spectrum, which can be deduced from the IPCE graph (inset Figure 7).[14]

For all the composition studied here, except pure $FAPbI_3$, c.a 80-85% light to electricity conversion can be observed in the visible part of the spectra. The incident photon-to-current efficiency (IPCE) measurement region was recorded in the wavelength range of 300-850 nm, where the perovskite solar cells showed photo conversion. This indicates that excitons and/or free charges were effectively generated in the perovskite layers upon light illumination. In case of pure $FAPbI_3$, the rapid degradation of devices did not permit the measurement of good IPCE spectrum.

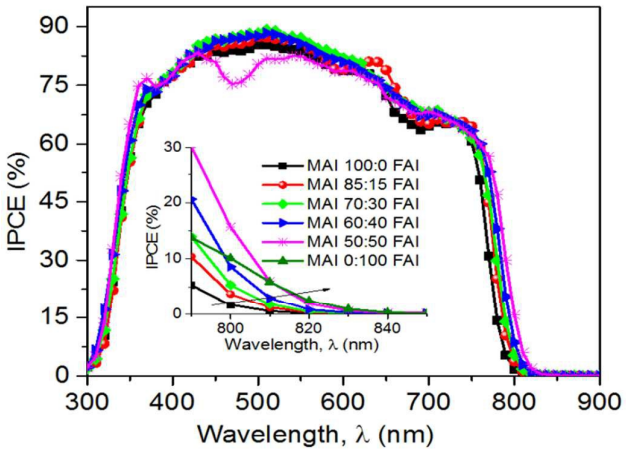

Figure 7. Incident photon-to-current efficiency of the devices.

Impedance measurements

To understand the correlation between charge carrier extraction dynamics and crystallographic properties of perovskite films, we performed Impedance spectroscopy (IS) which provides information concerning the performance of the perovskite solar cells at different charge-carrier densities.[57] Previous reports suggest the device architecture and particularly the perovskite layer play an important role in the interpretation of the impedance response.[58] Thus, to study the charge dynamics of the different layers in the devices, samples were analysed from maximum power point voltage to lower voltage. The measurements were performed by varying the illumination intensity at open-circuit voltage condition. On increase of the light intensity, charge carrier concentration increases and increment in V_{oc} is obtained. An equivalent circuit used for the fitting[60] of impedance measurement is shown in Figure S9.

For this reason it is important that a representative impedance model is established for mesoscopic perovskite solar cell devices. As reported, the hysteresis behaviour of the device is linked to the dielectric properties of the perovskite material.[59] Device capacitance is an important parameter to explain the mechanisms which control undesired effects such as hysteresis behaviour.[61] Recently Bisquert[62] reported how the acceptance or release of additional charges has repercussion in capacitance due to the change in the Fermi level of the system. The authors found that capacitance is independent of voltage or both interfaces (perovskite/TiO_2 or perovskite/Spiro-OMeTAD) but on the perovskite layer itself. Capacitance reflects the density of states (DOS) of a material, and thus high value in perovskite shows a high DOS. Figure 8 illustrates the value of capacitance for different organic cation composition in perovskite solar cells. The capacitance is almost independent of the applied voltage and depending on the ratio, they possess different capacitance value. Here also, the 60:40 ratio shows the lowest capacitance value, which is in agreement with the lowest hysteresis. As it is well known, semicircle observed in the impedance spectra, is related with diffusion-recombination process. In all cases, the magnitude of the impedance response generally increases with a decrease in the applied voltage. This trend is easily explained because an increase of voltage, entail a reduction of the recombination resistance, therefore the size of the semicircle. Nyquist plot (Figure S10), shows the existence of a unique semicircle or two depending on the perovskite configuration solar cells. Accordingly, it has been suggested that the distinct impedance features may originate from a distribution of trapping states within the perovskite band gap due to the inclusion of formamidinium cations in the structure.

Table 1: Average Photovoltaic parameters and calculated hysteresis index (HI) of the devices under 100 mW / cm^2. The scan direction was reverse that is from V_{oc} to J_{sc}, starts at 1.1 -0 *V* and back to 1.1 *V*. The values in parentheses were reported for the best devices.

PCCP

ARTICLE

Organic cation ratio	Annealing T(ºC)	R_s ohm cm^2	R_{sh} ohm cm^2	J_{SC} ($mA.cm^{-2}$)	V_{OC} (V)	*FF* (%)	PCE (%)	HI
MAI 100:FAI 0	100	5.10	1487.48	19.57±0.74 (19.79)	0.95±0.03 (0.987)	64.79±6.37 (74.18)	12.11±0.97 (14.49)	0.16
MAI 85:FAI 15	100	4.93	7947.37	19.78±0.07(19.90)	0.97±0.01(0.994)	70.61±1.69(73.32)	13.62±0.42 (14.50)	0.10
MAI 70:FAI 30	100	5.40	9033.63	19.69±0.36 (19.84)	0.89±0.01 (0.899)	66.63±3.21 (71.39)	11.85±0.58 (12.73)	0.05
MAI 60:FAI 40	100	5.25	3738.2	20.99±0.32 (20.873)	0.983±0.01 (0.975)	69.26±1.17 (69.97)	14.30±0.49 (14.23)	0.005
MAI 50:FAI 50	120	12.62	591.603	16.64±2.36 (19.92)	0.86±0.02 (0.929)	56.77±6.33 (54.99)	8.16±1.54 (10.18)	0.28
MAI15:FAI85	150	6.18	882.08	17.55	0. 802	65.5	9.22	0.12
MAI 0:FAI 100	150	10.50	1461.65	13.91±1.60 (15.66)	0.75±0.02 (0.805)	52.01±2.95 (59.80)	5.42±1.00 (7.53)	0.20

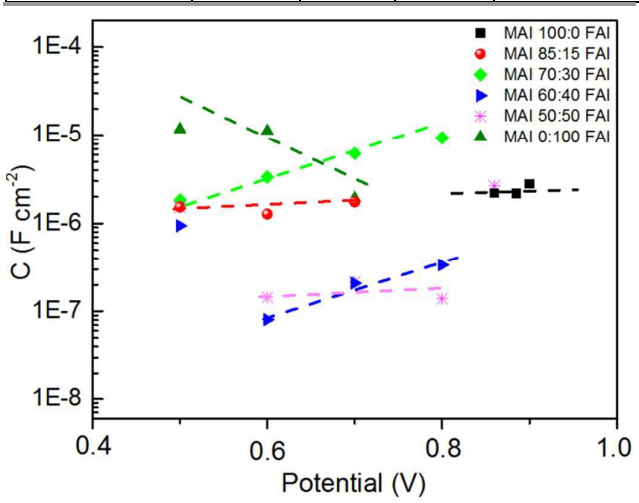

Figure 8. Capacitance values for $MA_xFA_{(1-x)}PbI_3$. Dash lines serve as a visual aid only. Impedance measurements were performed at open-circuit in the 2 -50 MHz frequency range. The equivalent circuit used, and the typical impedance spectra, are shown in Figure S8.

Stability

The low stability of perovskite based solar cells under high moisture is the current bottleneck in order to up-scale this technology. In general, the critical step in the fabrication of the devices is the perovskite layer deposition. A perovskite film deposited under controlled conditions exhibits good pinhole-free film coverage, in addition some researchers indicate that a small percentage (less than 30%) of humidity during the fabrication process also could be beneficial to accelerate the growth of perovskite crystals in order to obtain an homogeneous film.[63-65] Mainly, this instability is based on the facile phase transitions at room temperature and formation of hydrated phases owing to it hydrophilic character. The formamidinium cation exhibits lower stability than methylammonium, however the presence of smaller MA cation in mixed perovskite with FA improves stability even in high humidity conditions, which could be attributed to ten times higher dipole moment of small sized MA cation than FA. This MA stabilizes the 3D network of PbI_6 octahedra through hydrogen bonding between hydrogen of ammonium moiety and iodide ions or another possible reason of stability is strong coulomb interaction between the MA cation and PbI_6 octahedra.[20]

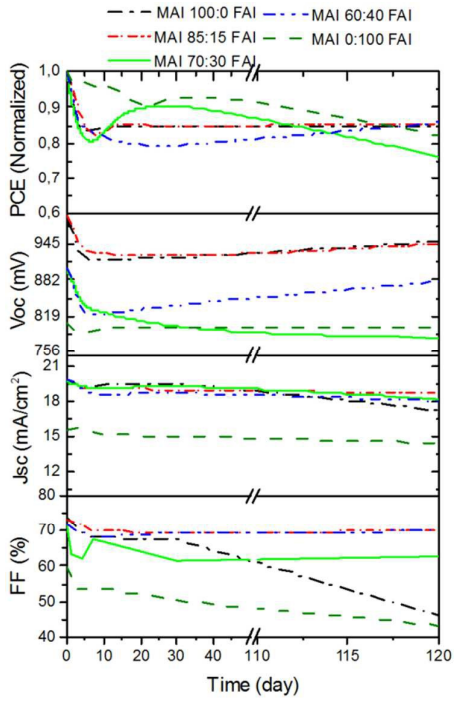

Figure 9. Evolution of stability data for the solar cells with different organic cation ratio, samples keep stables under humidity conditions (65%RH).

Figure 9 represents the evolution of the characteristic solar cell parameters V_{oc}, J_{sc} and FF, PCE plotted as a function of time to evaluate the stability of the fabricated perovskite solar cells using the mixed MAI:FAI ratio. The un-encapsulated devices were kept in the dark under high humidity level (>60% RH) and monitored by measuring *J-V* characteristics for different composition mixed cation perovskites. In general, the devices were found to be relatively stable, and in some cases, the device performance was found to be increased after 5 days of storage, this we assign to the improved intimate contact with the perovskites and HTM, or better infiltration of active materials inside the three dimensional TiO_2 structure. However, in most of the cases the device performance stabilizes after 10 days and relatively uniform output can be observed. It was noted that the substitution by FA into MA induce perovskite stability. PCE stable values were exposed for x=0.85 composition, after 5 days. The calculated drop in PCE after a period of four months was only 14.41% (from 14.5% to 12.41%) was observed, while for the pure MAI and FAI, the drop was about 16.49 % and 17.87%, respectively.

Conclusions

To summarize, we have studied varying composition of mixed-cation perovskite $MA_xFA_{1-x}PbI_3$, where (x=0–1) for perovskite solar cells fabrication using one step solvent engineering approach. It was found that the addition of formamidinium cation in the MAI slows down the crystal formation in perovskites and allows the formation of large crystals and high degree of order. Devices fabricated using pure FAI gave the lowest performance here, while all the mixed and pure MAI shows superior PV performance. The addition of 15-40% FAI in MAI found to influence the PV performance and dramatically reduced the hysteresis behaviour. The mixed-cation perovskite $MA_{0.6}FA_{0.4}PbI_3$ exhibited hysteresis free behaviour along with the best PV performance. By using the solvoneering (solvent engineering) approach, we were able to fabricate devices >15% photon-to-current conversion efficiency under the AM1.5G simulated solar spectrum. The strategy of mixing organic ammonium compounds opens up new prospects for the further optimization and understanding of hysteresis free behaviour.

Experimental Section

All chemicals were procured from Sigma Aldrich and used as such, PbI_2 was obtained from TCI, while MAI and FAI were procured from Dyesol and employed without any treatment or purification. 2,2',7,7'-tetrakis(N,N-di-p-methoxyphenyamine)-9,9-spirobifluorene (Spiro-OMeTAD) was acquired from Merck KGaA.

Device fabrication

Perovskite solar cells were fabricated on FTO-coated glass (TEC15, Pilkington) patterned by laser etching. Before any deposition, the substrates were cleaned using Hellmanex solution and rinsed with deionized water and ethanol and finally ultrasonicated in 2-propanol and air dried. TiO_2 compact layer was deposited by spray pyrolysis at 450°C using 1mL of titanium diisopropoxide bis(acetyl acetonate) precursor solution (75% in 2-propanol, Sigma Aldrich) in 19mL of pure ethanol using dry air as carrier gas. After the blocking layer deposition, the substrates were kept for further 30 minutes at 450°C for the formation of anatase phase. Once the samples were cooled down at room temperature, they were treated with $TiCl_4$ (dipping in a 0.02M $TiCl_4$ solution in deionized water at 70°C for 30 minutes) with the aim to obtain a homogenous layer. Next, the samples were then washed with deionized water, burned at 500°C for 10 minutes and were cooled down to room temperature. After this, a TiO_2 mesoporous layer (Dyesol, 30NRD) was deposited by spin coating (4000 rpm for 30s) and then samples were heated progressively up to 450°C for 2 hours.

Atop of this, $MA_xFA_{1-x}PbI_3$ (x=0-1) was deposited by one step method followed by toluene solvoneering (solvent engineering) method. The solution and perovskite films were prepared inside an argon glove box with moisture and oxygen controlled conditions (H_2O level: <1ppm and O_2 level: <10ppm) and kept stirring at 80°C overnight in order to dissolved completely of PbI_2. Perovskite precursor solution composed of lead iodide (1.25M) (PbI_2) and a mixture of formamidinium iodide (FAI) and methyl ammonium iodide (MAI) were dissolved in dimethylsulfoxide (DMSO) and, precursor solution was spin coated on top of the mesoporous layer at 1000 rpm for 10 s and then 6000 rpm for 30s. During the second step, Toluene (900 µl) was dripped at the centre of the substrate in the last 15 seconds. After solvent treatment, the films were

transferred onto a hotplate and annealed at 100-150°C for 60 minutes depending on the cation composition. Spiro-OMeTAD was then spun coated at 4000 rpm for 30 s by dissolving 72.3 mg of Spiro-OMeTAD in 1 mL of chlorobenzene; 21.9 µL of tris(2-(1H-pyrazol-1-yl)-4-tert-butylpyrydine)cobalt(III) bis(trifluoromethylsulphonyl)imide (FK209) from stock solution (400 mg of FK209 in 1 mL of acetonitrile), 17.5 µL of lithium bis(trifluoromethylsulphonyl)imide (LiTFSI) stock solution (520 mg of LiTFSI in 1mL of acetonitrile) and 28.8 µL of 4-tert-butylpyridine were also added to the solution as dopants. Finally, 80 nm of gold (Au) were thermal evaporated on the top of the cell as cathode under a vacuum level between 1×10^{-6} and 1×10^{-5} torr.

Characterization

For structural characterization, thick films were prepared by spin coating of $MA_xFA_{(1-x)}PbI_3$ (x=0-1) solutions onto coarse glass. X-ray diffractograms were recorded on a Rigaku powder diffractometer using CuKα source. The measurements were performed in the Bragg-Brentano geometry. The samples were mounted without any further modification and the divergence slit were adjusted to the dimension of the films. A scan range from 10° to 60° was selected with an acquisition time of 1 degree/min. A baseline correction was applied to diffractograms to compensate for the noise arising from the substrate.

The Transmittance and reflectance spectra of the perovskite films were collected using Perkin Elmer UV-vis-NIR lambda 1050 spectrophotometer using 160 mm integrating sphere. Surface morphology and cross sectional images were obtained using Hitachi S-4800 field emission scanning electron microscope at power 2 kV.

Current density–voltage (*J–V*) curves were recorded with a Keithley 2400 source-measurement-unit under AM 1.5 G, 100 mW cm^2 illumination from a certified Class AAA, 450 W solar simulator (ORIEL, 94023 A). Light output power was calibrated using a NREL certified calibrated mono-crystalline silicon solar cell. A black metal mask (0.16 cm^2) was used over the square solar cell active area (0.5 cm^2) to reduce the influence of scattered light.

Photovoltaic parameters including J_{sc}, V_{oc}, fill factor (FF), and power conversion efficiency (PCE) were extracted from the photocurrent-voltage (*J-V*) curves of the solar cells and listed in Table 1. The scan rate and the active area used for measuring the devices were optimized as such to calculate the real value for efficiencies without having hysteresis effect. (Active area: 0.16 cm^2, scan rate: 100 mV/s, pre sweep delay: 20s). The IPCE measurements were performed using a Newport 150 W xenon lamp coupled to an Oriel Cornerstone 260 motorized ¼ m monochromator as the light source, and a 2936-R power meter to measure the short circuit current. The small perturbation measurements (EIS) were carried under illumination in order to approach the operation conditions for solar cells. Samples were illuminated by a 530 nm LED (LUXEON) over a wide range of DC light intensities. EIS spectra have been recorded with the application of a bias equal to the potential induced by the light. The bias close to V_{oc} and applied during the measurements was chosen to minimize the current running through the cell during the measurements and to avoid the voltage drop due to series resistance. Z-view (Scribner) was used for equivalent circuit modelling of the EIS spectra.

The surface of mixed cation perovskite were observed by top-view and cross-sectional Field-emission SEM, respectively, using a Hitachi S5200 field-emission microscope operating at 5.0 keV. SFM measurements were performed with an EnviroScope (Bruker Nano Surfaces) which allows controlling the environmental condition such as humidity, oxygen content and sample temperature. The samples were deposited on glass substrates following the procedure described above. The glass substrates were much smoother than the FTO substrates. Therefore the roughness of the perovskite layers could be measured more accurately.

Acknowledgements

This project has received funding from the European Union Seventh Framework Programme under grant agreement n° 607232 [THINFACE]."

Keywords: Perovskite solar cells •Mixed organic cation• Formamidinium lead iodide •Methyl ammonium lead iodide •Hysteresis

Notes and references

1 B. O'Regan and M. Grätzel, *Nature*, 1991, **353**, 737–740.
2 A. Kojima, K. Teshima, Y. Shirai and T. Miyasaka, *J. Am. Chem. Soc.*, 2009, **131**, 6050–6051.
3 M. Grätzel, R. A. J. Janssen, D. B. Mitzi and E. H. Sargent, *Nature*, 2012, **488**, 304–12.
4 S. Kazim, M. K. Nazeeruddin, M. Grätzel and S. Ahmad, *Angew. Chemie - Int. Ed.*, 2014, **53**, 2812–2824; Angew Chem. 2014, **126**, 2854-2867.
5 X. Liu, W. Zhao, H. Cui, Y. Xie, Y. Wang, T. Xu and F. Huang, *Inorg. Chem. Front.*, 2015, **2**, 315–335.
6 S. Brittman, G. W. P. Adhyaksa and E. C. Garnett, *MRS Commun.*, 2015, **5**, 7–26.
7 V. M. Goldschmidt, *Naturwissenschaften*, 1926, **14**, 477–485.
8 G. E. Eperon, S. D. Stranks, C. Menelaou, M. B. Johnston, L. M. Herz and H. J. Snaith, *Energy Environ. Sci.*, 2014, **7**, 982.
9 J.-W. Lee, D.-J. Seol, A.-N. Cho and N.-G. Park, *Adv. Mater.*, 2014, **6**, 1–8.
10 G. E. Eperon, C. E. Beck and H. J. Snaith, *Mater. Horiz.*, 2016, **3**, 63–71.
11 P. Piatkowski, B. Cohen, C. S. Ponseca, M. Salado, S. Kazim, S. Ahmad, V. Sundström and A. Douhal, *J. Phys. Chem. Lett.*, 2015, **7**, 204–210.
12 V. Adinolfi, M. Yuan, R. Comin, E. S. Thibau, D. Shi, M. I. Saidaminov, P. Kanjanaboos, D. Kopilovic, S. Hoogland, Z.-H. Lu, O. M. Bakr and E. H. Sargent, *Adv. Mater*.2016, **28**, 3406–3410.
13 A.A. Zhumekenov, M.I. Saidaminov, M. A. Haque, E. Alarousu, S. P. Sarmah, B. Murali, I. Dursun, X.-H. Miao, A. L. Abdelhady, T. Wu, O. F. Mohammed, and O. M. Bakr, *ACS Energy Lett*. 2016, **1**, 32−37.
14 N. Pellet, P. Gao, G. Gregori, T.-Y. Yang, M. K. Nazeeruddin, J. Maier and M. Grätzel, *Angew. Chem. Int. Ed. Engl.*, 2014, **53**, 3151–7.
15 S. Pang, H. Hu, J. Zhang, S. Lv, Y. Yu, F. Wei, T. Qin, H. Xu, Z. Liu and G. Cui, *Chem. Mater.*, 2014, **26**, 1485–1491.

16 J. Burschka, N. Pellet, S.-J. Moon, R. Humphry-Baker, P. Gao, M. K. Nazeeruddin and M. Grätzel, *Nature*, 2013, **499**, 316–320.
17 M. Liu, M. B. Johnston and H. J. Snaith, *Nature*, 2013, **501**, 395–8.
18 Q. Chen, H. Zhou, Z. Hong, S. Luo, H. S. Duan, H. H. Wang, Y. Liu, G. Li and Y. Yang, *J. Am. Chem. Soc.*, 2014, **136**, 622–625.
19 N. J. Jeon, J. H. Noh, Y. C. Kim, W. S. Yang, S. Ryu and S. Il Seok, *Nat. Mater.*, 2014, **13**, 897–903.
20 A. Binek, F. C. Hanusch, P. Docampo and T. Bein, *J. Phys. Chem. Lett.*, 2015, **6**, 1249–1253.
21 J. Liu, Y. Shirai, X. Yang, Y. Yue, W. Chen, Y. Wu, A. Islam and L. Han, *Adv. Mater.*, 2015, **27**, 4918–4923.
22 C. C. Stoumpos, C. D. Malliakas and M. G. Kanatzidis, *Inorg. Chem.*, 2013, **52**, 9019–9038.
23 T.J. Jacobsson, J. P. Correa-Baena, M. Pazoki, M Saliba, K. Schenk, M. Grätzel, A. Hagfeldt, *Energy Environ. Sci.*, 2016, **9**, 1706-1724.
24 M. T. Weller, O. J. Weber, J. M. Frost and A. Walsh, *J. Phys. Chem. Lett.*, 2015, **6**, 3209–3212.
25 D. H. Cao, C. C. Stoumpos, C. D. Malliakas, M. J. Katz, O. K. Farha, J. T. Hupp, M. G. Kanatzidis, *APL Mater.* **2014**, *2*, 091101.
26 P. Using, X. Di, T. J. Jacobsson, L. J. Schwan, M. Ottosson, A. Hagfeldt and T. Edvinsson, *Inorg. Chem. Front.*, 2015, **54**, 10678–10685.
27 S. Aharon, A. Dymshits, A. Rotem and L. Etgar, *J. Mater. Chem. A*, **2015**, *3* , 9171.
28 Y. Chen, J. He, Y. S. Peng and L. Ziqi, *Adv. Sci.*, 2016, **3**, doi: 10.1002/advs.201500392.
29 J. M. Ball, M. M. Lee, A. Hey and H. J. Snaith, *Energy Environ. Sci.*, 2013, **6**, 1739.
30 V. D'Innocenzo, A. R. Srimath Kandada, M. De Bastiani, M. Gandini and A. Petrozza, *J. Am. Chem. Soc.*, 2014, **136**, 17730–17733.
31 G. Grancini, S. Marras, M. Prato, C. Giannini, C. Quarti, F. De Angelis, M. De Bastiani, G. E. Eperon, H. J. Snaith, L. Manna and A. Petrozza, *J. Phys. Chem. Lett.*, 2014, **5**, 3836–3842.
32 D. J. Seol, J. W. Lee and N. G. Park, *ChemSusChem*, 2015, **8**, 2414–2419.
33 L. Wang, C. McCleese, A. Kovalsky, Y. Zhao and C. Burda, *J. Am. Chem. Soc.*, 2014, **110**, 12205–12208.
34 Y. Yamada, T. Nakamura, M. Endo, A. Wakamiya and Y. Kanemitsu, *J. Am. Chem. Soc.*, 2014, **136**, 11610–3.
35 S. D. Stranks, V. M. Burlakov, T. Leijtens, J. M. Ball, A. Goriely and H. J. Snaith, *Phys. Rev. Appl.*, 2014, **2,** 034007.
36 G. J. A. H. Wetzelaer, M. Scheepers, A. M. Sempere, C. Momblona, J. Ávila and H. J. Bolink, *Adv. Mater.*, 2015, **27**, 1837–1841.
37 W. Tress, N. Marinova, O. Inganäs, M. K. Nazeeruddin, S. M. Zakeeruddin and M. Graetzel, *Adv. Energy Mater.*, 2015, **5**.
38 N. Marinova, W. Tress, R. Humphry-Baker, M. I. Dar, V. Bojinov, S. M. Zakeeruddin, M. K. Nazeeruddin and M. Grätzel, *ACS Nano*, 2015, **9**, 4200–4209.
39 S. D. Stranks, G. E. Eperon, G. Grancini, C. Menelaou, M. J. P. Alcocer, T. Leijtens, L. M. Herz, A. Petrozza and H. J. Snaith, *Science*, 2013, **342**, 341–344.
40 G. Xing, N. Mathews, S. Sun, S. S. Lim, Y. M. Lam, M. Grätzel, S. Mhaisalkar and T. C. Sum, *Science* , 2013, **342**, 344–347.
41 P. W. Liang, C. Y. Liao, C. C. Chueh, F. Zuo, S. T. Williams, X. K. Xin, J. Lin and A. K. Y. Jen, *Adv. Mater.*, 2014, **26**, 3748–3754.
42 Y. Wu, A. Islam, X. Yang, C. Qin, J. Liu, K. Zhang, W. Peng and L. Han, *Energy Environ. Sci.*, 2014, **7**, 2934.
43 P. Docampo, F. C. Hanusch, S. D. Stranks, M. Döblinger, J. M. Feckl, M. Ehrensperger, N. K. Minar, M. B. Johnston, H. J. Snaith and T. Bein, *Adv. Energy Mater.*, 2014, **4**, 1400355.
44 Z. Xiao, C. Bi, Y. Shao, Q. Dong, Q. Wang, Y. Yuan, C. Wang, Y. Gao and J. Huang, *Energy Environ. Sci.*, 2014, **7**, 2619.
45 J. You, Y. (Michael) Yang, Z. Hong, T.-B. Song, L. Meng, Y. Liu, C. Jiang, H. Zhou, W.-H. Chang, G. Li and Y. Yang, *Appl. Phys. Lett.*, 2014, **105**, 183902.
46 P. F. Ndione, W.-J. Yin, K. Zhu, S.-H. Wei and J. J. Berry, *J. Mater. Chem. A*, 2015, 3, 21940-21945.
47 D. Li, S. A. Bretschneider, V. W. Bergmann, I. M. Hermes, J. Mars, A. Klasen, H. Lu, W. Tremel, M. Mezger, H.-J. Butt, S. A. L. Weber and R. Berger, *J. Phys. Chem. C*, 2016, **120**, 6363–6368.
48 H. S. Kim and N.-G. Park, *J. Phys. Chem. Lett.*, 2014, **5**, 2927–2934.
49 R. S. Sanchez, V. Gonzalez-Pedro, J. W. Lee, N. G. Park, Y. S. Kang, I. Mora-Sero and J. Bisquert, *J. Phys. Chem. Lett.*, 2014, **5**, 2357–2363.
50 H. J. Snaith, A. Abate, J. M. Ball, G. E. Eperon, T. Leijtens, N. K. Noel, S. D. Stranks, J. T. W. Wang, K. Wojciechowski and W. Zhang, *J. Phys. Chem. Lett.*, 2014, **5**, 1511–1515.
51 S. Van Reenen, M. Kemerink and H. J. Snaith, *J. Phys. Chem. Lett.*, 2015, **6**, 3808–3814.
52 B. Chen, M. Yang, X. Zheng, C. Wu, W. Li, Y. Yan, J. Bisquert, G. Garcia-Belmonte, K. Zhu and S. Priya, *J. Phys. Chem. Lett.*, 2015, **6**, 4693–4700.
53 C. Motta, F. El-Mellouhi, S. Kais, N. Tabet, F. Alharbi and S. Sanvito, *Nat. Commun.*, 2015, **6**, 7026.
54 Y. Yuan and J. Huang, *Acc. Chem. Res.*, 2015, **49**, 286–293.
55 J. J. Choi, X. Yang, Z. M. Norman, S. J. L. Billinge and J. S. Owen, *Nano Lett.*, 2014, **14**, 127–33.
56 M. B. Johnston and L. M. Herz, *Acc. Chem. Res.*, 2015, **49**, 146–154.
57 E. Guillén, F. J. Ramos, J. A. Anta and S. Ahmad, *J. Phys. Chem. C*, 2014, **118**, 22913–22922.
58 A. R. Pascoe, N. W. Duffy, A. D. Scully, F. Huang and Y.-B. Cheng, *J. Phys. Chem. C*, 2015, **119**, 4444–4453.
59 E. J. Juarez-Perez, R. S. Sanchez, L. Badia, G. Garcia-Belmonte, Y. S. Kang, I. Mora-Sero and J. Bisquert, *J. Phys. Chem. Lett.*, 2014, **5**, 2390–2394.
60 J. Bisquert, L. Bertoluzzi, I. Mora-sero and G. Garcia-belmonte, *J. Phys. Chem. C*, 2014, **118**, 18983–18991.
61 O. Almora, I. Zarazua, E. Mas-Marza, I. Mora-Sero, J. Bisquert and G. Garcia-Belmonte, *J. Phys. Chem. Lett.*, 2015, **6**, 1645–1652.
62 J. Bisquert, *Phys. Chem. Chem. Phys.*, 2003, **5**, 5360.
63 H. Zhou, Q. Chen, G. Li, S. Luo, T. -b. Song, H.-S. Duan, Z. Hong, J. You, Y. Liu and Y. Yang, *Science*, 2014, **345**, 542–546.
64 T. Leijtens, G. E. Eperon, N. K. Noel, S. N. Habisreutinger, A. Petrozza and H. J. Snaith, *Adv. Energy Mater.*, 2015, **5,** 1500563.
65 N.-G. Park, *Mater. Today*, 2015, **18**,65-72.

Table of content:

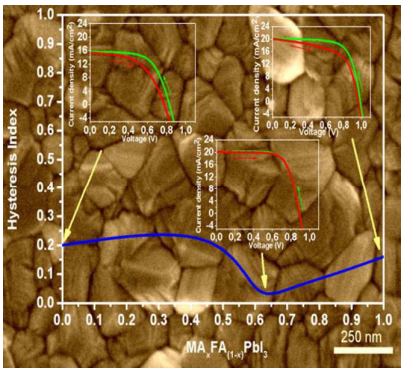

Perovskite solar cells were fabricated using mixed organic cation of formamidinium and methylammonium cation. Mixed cation having composition $MA_{0.6}FA_{0.4}PbI_3$ shows almost negligible *I–V* hysteresis and better photostability than pure $MAPbI_3$ and $FAPbI_3$.